processes

MDPI

Article

Mathematical Investigation of Heat Transfer Characteristics and Parameter Optimization of Integral Rolled Spiral Finned Tube Bundle Heat Exchangers

Danfeng Zhang [1,2], Wenchang Wu [1,2], Liang Zhao [1,2,*] and Hui Dong [1,2]

[1] State Environmental Protection Key Laboratory of Eco-Industry, Northeastern University, Shenyang 110819, China
[2] Liaoning Engineering Research Center of Energy Saving and Green Low Carbon Technology for Process Industry, Shenyang 110819, China
* Correspondence: zhliang8341@163.com

Abstract: In this study, the effects of fin tip thickness and fin root thickness of integral rolled spiral finned tube bundles on flow resistance, heat transfer performance and heat transfer and flow exergy destruction were investigated via mathematical simulation. The correlations between heat transfer and flow resistance performance were fitted with dimensionless numbers. The optimized parameters with performance evaluation criteria (PEC) as the objective were obtained using methods involving computational fluid dynamics and machine learning. The results show the effects of fin tip thickness and fin root thickness on the Nusselt number (*Nu*), Euler number (*Eu*), PEC, heat transfer exergy destruction (*ExT*) and flow exergy destruction (*ExP*) as obtained via mathematical simulation. A new mathematical correlation is proposed for predicting the *Nu* and *Eu* of integral rolled spiral finned tube bundles. Among the four optimization models tested, the random forest regression algorithm was the most accurate algorithm for PEC prediction models. In the studied range, the optimal parameters were a fin tip thickness of 2 mm and a fin root thickness of 3.5 mm. Compared with the initial parameters, when the Reynolds number was 20,380, the PEC increased by 2.53%, the *ExP* increased by 2.37% and the *ExT* decreased by 7.96%.

Keywords: integral rolled spiral finned tube; heat transfer characteristics; parameter optimization; performance evaluation criteria; exergy destruction minimization principle

Citation: Zhang, D.; Wu, W.; Zhao, L.; Dong, H. Mathematical Investigation of Heat Transfer Characteristics and Parameter Optimization of Integral Rolled Spiral Finned Tube Bundle Heat Exchangers. *Processes* **2023**, *11*, 2192. https://doi.org/10.3390/pr11072192

Academic Editor: Alfredo Iranzo

Received: 25 April 2023
Revised: 9 June 2023
Accepted: 11 July 2023
Published: 21 July 2023

1. Introduction

Heat exchangers are heat transfer devices that transfer heat from high-temperature fluids to low-temperature fluids, and they are usually used to recover waste heat. Heat exchangers are widely used in the power, refrigeration, metallurgy, chemical, food, paper, petroleum and aerospace industries [1–4]. Improvements to the performance and efficiency of heat exchangers and the design of heat exchanger equipment for industrial production have important economic and social significance in increasing energy shortages. At present, heat exchanger enhancement techniques mainly include active and passive heat transfer enhancement techniques, which mainly depend on whether additional energy is provided [5–7]. Compared with active heat transfer enhancement techniques, passive heat transfer enhancement techniques do not provide external energy in the improvement process, which is why they have lower costs and wider applications. The passive heat transfer enhancement technique is used to enhance the flow field disturbance near the surface of tube bundle and generate a secondary flow and vortex by changing the geometric model of the outside of the tube bundle. The spiral fin [8–10], L-footed spiral fin [11,12], crimped spiral fin [13–15] and serrated spiral fin designs [16,17] are representatives of this method. The other method is to improve the heat transfer characteristics of the tube bundle by changing its manufacturing process. The most common finned tube bundles are made using high-frequency welding technology in industry. The integral rolling technique involves rolling thick-walled seamless steel tubes into finned tubes with fixed parameters at 900–950 °C, which has the advantages of good shock resistance, long service time, good resistance to ash deposition and no thermal contact resistance.

There is no doubt that current heat exchanger enhancement technology can improve the heat transfer capacity of tube bundles, but they increase flow resistance at the same time, which can increase the power necessary for pumps and fans. Therefore, increasing the heat transfer capacity of the tube bundle alone cannot enhance the comprehensive performance of the tube bundle. It is necessary to comprehensively consider the heat transfer capacity and the flow resistance of tube bundles. Many researchers have evaluated the comprehensive heat transfer capacity of tube bundles by using the performance evaluation criteria (PEC) [18–21], j/f factor [22–26] and other evaluation indexes based on the first law of thermodynamics. However, evaluation indexes based on the first law of thermodynamics only consider the quantitative characteristics of heat transfer (such as temperature and heat flow, etc.); they do not consider the efficiency of heat transfer. It is not only necessary to comprehensively consider the enhancement of heat transfer but also to find ways to reduce irreversible loss and power consumption in the heat transfer process. Therefore, many researchers have proposed new evaluation indexes based on the second law of thermodynamics, such as the entransy dissipation extremum principles (EDEP) [27–29], the exergy destruction minimization principle (EDMP) [30–33], the entropy generation minimization principle (EGMP) [34–37], etc. The EDMP, proposed by Liu et al. [30], can not only evaluate irreversible loss in the heat transfer process but also describe the flow loss caused by the fluid flow process. The exergy loss caused by heat transfer represents the loss of available energy, and the exergy loss caused by fluid flow represents the power consumed by the pump and fan, which can also be called the loss of mechanical energy. In recent years, several researchers [31–33] have expanded the use of EDMP to make it more generalizable. In slotted fin designs, Wang et al. [31] investigated the effect of fin slot parameters on heat transfer and flow exergy destruction, and they obtained optimized parameters using a neural network and a genetic algorithm. Xiao et al. [32] mathematically extended the exergy destruction minimization principle to three-dimensional turbulent flow and derived governing equations with the variation method. They improved the thermal–hydraulic performance of a solar air heater with the optimization approach. Xie et al. [33] studied the heat transfer and flow characteristics of helical micro-fin tubes via mathematical simulation and proved that the minimum exergy loss principle is applicable to the periodic model and with fully developed turbulence.

In order to enhance the waste heat recovery capacity of the heat recovery steam generator (HRSG) and the combined cycle power plant (CCPP), passive heat transfer enhancement techniques are used to enhance the heat transfer capacity of heat exchanges in the HRSG. The effect of fin height, fin pitch, transverse pitch and longitudinal pitch on the heat transfer and flow resistance characteristics of the integral rolled spiral finned tube bundles was experimentally investigated in the context of the final stage economizer in the HRSG of a CCPP. However, to the best of our knowledge, the existing research results regarding integral finned tubes cannot be directly applied to integral rolled spiral finned tubes for the following reasons: (1) the research fields (air conditioning, refrigeration and heat recovery steam generators); (2) the material and structure of the fins (aluminum and low-carbon steel); and (3) the working conditions. Therefore, in order to better apply the integral rolled spiral finned tube design to the HRSG of a CCPP, it is still necessary to study the structural parameters of the integral rolled spiral finned tube (fin tip thickness and fin root thickness) on the heat transfer and resistance characteristics of the tube bundles.

Based on the above research, this work was intended to study the influence of tip thickness and fin root thickness on the comprehensive performance of the integral rolled spiral finned tube bundles based on the valuation indexes of the first law and the second law of thermodynamics via mathematical calculation. The optimization algorithm is used to find the optimal fin tip thickness and fin root thickness parameters by taking PEC as the optimization objective. This work fills the gap in the study of flow resistance and heat transfer characteristics of integral rolled spiral finned tube bundles based on the second law of thermodynamics. The results are of great significance to improve the comprehensive heat transfer performance of HRSG in a CCPP.

2. Mathematical Simulation

2.1. Physical Model

In order to save computing resources and retain the characteristics of gas flow resistance and heat transfer, part of the experimental equipment is determined as the physical model, and the inner part of the red frame is selected as the calculation domain of the mathematical simulation in Figure 1. The Ansys Fluent 19.2 is used for the mathematical simulation. The Design Modeler is used for building physical models, and the Meshing is used for grids. The central dark part is the solid fin domain, while the upper and lower regions are the gas domain surrounding the solid fin domain. The fluid water domain is surrounded by the solid fin domain. It can be clearly shown that the upper and lower surfaces are set as periodic boundaries, and the left and right surfaces are set as symmetrical boundaries. The intersection of the gas domain and the solid fin domain is set as a solid–fluid coupled interface. The contact surface between the inner wall of the pipe and the fluid water domain is set as no-slip condition. The gas and water are set as the velocity inlet and pressure outlet, respectively. In order to ensure the uniformity of gas inlet velocity and avoid the influence of backflow at the outlet, the inlet extends 300 mm upstream and the outlet extends 800 mm downstream. The fin parameters and boundary conditions are consistent with the experimental conditions, as shown in Table 1. The parameter equations of the working substance are obtained by fitting the data from the NIST database [38]. The values of R^2 for the parameter equations are greater than 0.99.

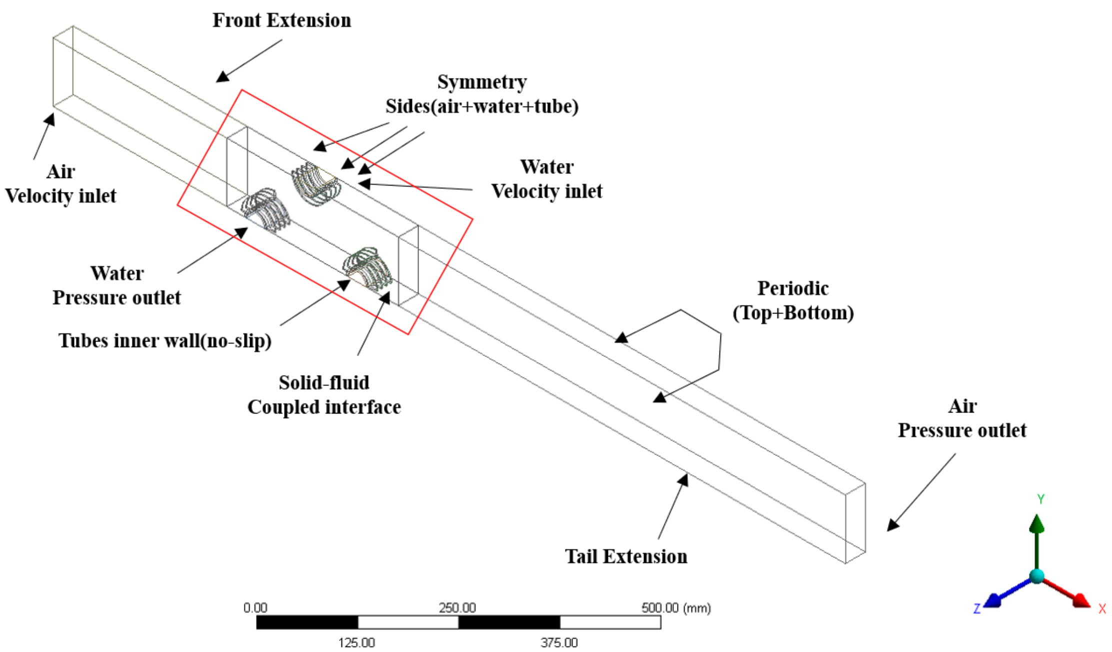

Figure 1. Simulated model and boundary conditions of finned tube bundles.

Table 1. Parameters and boundary conditions.

	Value/Unit		Value/Unit
Fin parameters			
δ_1	1.8 mm	S_{L}	104 mm
δ_2	3.5 mm	p_{f}	8 mm
h_{f}	12.8 mm	Front extension	300 mm
S_{T}	89 mm	Tail extension	800 mm
d_{i}	32 mm	d_{o}	38 mm
Boundary conditions			
$u_{\mathrm{g,i}}$	3.3–12.3 m/s	$u_{\mathrm{w,i}}$	0.3 m/s
$T_{\mathrm{g,i}}$	422.75 K	$T_{\mathrm{w,i}}$	293.15 K
Parameters of the working substance			
ρ_{g}	$\mathrm{y} = -3 \times 10^{-9} T_{\mathrm{g}}^3 + 7 \times 10^{-6} T_{\mathrm{g}}^2 - 0.0067 T_{\mathrm{g}} + 2.5547$ (kg/m^3)		
Cp_{g}	$\mathrm{y} = -2 \times 10^{-7} T_{\mathrm{g}}^3 + 0.0005 T_{\mathrm{g}}^2 - 0.1354 T_{\mathrm{g}} + 1054.8$ (J/kg·K)		
λ_{g}	$\mathrm{y} = 1 \times 10^{-8} T_{\mathrm{g}}^2 + 8 \times 10^{-5} T_{\mathrm{g}} + 0.003$ (W/m·K)		
μ_{g}	$\mathrm{y} = 1 \times 10^{-11} T_{\mathrm{g}}^2 + 5 \times 10^{-8} T_{\mathrm{g}} + 3 \times 10^{-6}$ (Pa·s)		
ρ_{w}	$\mathrm{y} = -0.0033 T_{\mathrm{g}}^2 + 1.6988 T_{\mathrm{g}} + 783.59$ (kg/m^3)		
Cp_{w}	$\mathrm{y} = -8 \times 10^{-5} T_{\mathrm{g}}^3 + 0.0902 T_{\mathrm{g}}^2 - 32.855 T_{\mathrm{g}} + 8088.2$ (J/kg·K)		
λ_{w}	$\mathrm{y} = -9 \times 10^{-6} T_{\mathrm{g}}^2 + 0.0069 T_{\mathrm{g}} - 0.6673$ (W/m·K)		
μ_{w}	$\mathrm{y} = -2 \times 10^{-9} T_{\mathrm{g}}^3 + 2 \times 10^{-6} T_{\mathrm{g}}^2 - 0.0007 T_{\mathrm{g}} + 0.082$ (Pa·s)		

2.2. Governing Equations

The three-dimensional steady-state, turbulent flow and heat transfer characteristics of the integral rolled spiral finned tube bundles are studied via mathematical simulation. The fluid flow and heat transfer processes are described by the Euler method. The assumptions and simplifications are described as follows:

(1) The processes of flow and heat transfer are steady state;
(2) The fluid is incompressible ideal fluid;
(3) The volume force only considers gravity;
(4) The effect of radiation heat transfer on the processes of flow and heat transfer is ignored.
(5) The parameters of the finned tube are set as the constant.

The heat transfer processes include: (1) the convective heat transfer between the high temperature fluid and the outer surface of the finned tube; (2) the heat conduction from the outer surface to the inner surface of the finned tube; and (3) the convective heat transfer between the inner surface of the finned tube and the low temperature fluid in the tube. The fluid–solid coupling heat transfer and the heat conduction inside the finned tube are considered in the mathematical calculation. The continuity, momentum and energy equations are as follows:

The continuity equation:

$$\frac{\partial(\rho u_i)}{\partial x_i} = 0 \tag{1}$$

The momentum equation:

$$\frac{\partial}{\partial x_i}(\rho u_i u_k) = \frac{\partial}{\partial x_i}\left(\mu \frac{\partial u_k}{\partial x_i}\right) - \frac{\partial p}{\partial x_k} + \rho g_i \tag{2}$$

The energy equation:

$$\frac{\partial}{\partial x_i}(\rho u_i T) = \frac{\partial}{\partial x_i}\left(\frac{k_1}{C_p}\frac{\partial T}{\partial x_i}\right) \tag{3}$$

$$k_1 = \frac{1}{\frac{1}{h_1} + \frac{\delta}{\lambda} + \frac{1}{h_2}} \tag{4}$$

For solid regions:

$$\frac{\partial}{\partial x_i}\left(\lambda \frac{\partial T}{\partial x_i}\right) = 0 \tag{5}$$

where h_1 is the convective heat transfer coefficient between the gas and the outer surface of the finned tube, δ is the finned tube wall thickness, h_2 is the convective heat transfer coefficient between the fluid in the tube and the inner surface of the finned tube, and k_1 is the comprehensive heat transfer coefficient.

The choice of turbulence model has an impact on the results of mathematical calculations of the gas flow and heat transfer process in the integral rolled spiral finned tube bundles. Therefore, selecting the appropriate turbulence model is helpful to improve the accuracy of mathematical calculations and reduce the calculation cost. The k-ε models [39–41] are commonly used to simulate the heat transfer and flow processes in tube bundles. The Realizable k-ε model is selected for the wide applicability and high accuracy.

The governing equations of k and ε in the turbulence model are as follows:

Kinetic energy equation:

$$\frac{\partial}{\partial x_j}(\rho k u_j) = \frac{\partial}{\partial x_j}\left[\left(\mu + \frac{\mu_t}{\sigma_k}\right)\frac{\partial k}{\partial x_j}\right] + G_k - \rho\varepsilon \tag{6}$$

Dissipation rate equation:

$$\frac{\partial}{\partial x_j}(\rho \varepsilon u_j) = \frac{\partial}{\partial x_j}\left[\left(\mu + \frac{\mu_t}{\sigma_\varepsilon}\right)\frac{\partial \varepsilon}{\partial x_j}\right] + \rho C_1 S\varepsilon - \rho C_2 \frac{\varepsilon^2}{k + \sqrt{v\varepsilon}} \tag{7}$$

$$G_k = -\rho\overline{u_j' u_i'}\frac{\partial u_i}{\partial x_j} \tag{8}$$

$$\mu_t = \rho C_\mu \frac{k^2}{\varepsilon} \tag{9}$$

where σ_k = 1.0 and σ_ε = 1.2 are the Prandtl numbers for k and ε, respectively. C_1 = 1.44, C_2 = 1.92, and C_μ = 0.09 are used in the mathematical simulation.

2.3. Grid Independence Verification

The physical mesh model and details are shown in Figure 2. The hexahedral structured grid is mainly used to mesh the geometric model. The geometric model with the structural parameters of the fin tip thickness of 1.8 mm and the fin root thickness of 3.5 mm is selected. Five different grid systems are generated in Table 2. In order to eliminate the influence of the number of grids on the calculation results, the *Nu* of different grid systems is compared under the same boundary conditions (*Re* = 5660). The results show that *Nu* increases with the increase in the number of grids. When the number of grids increases from case 4 to case 5, the *Nu* has no obvious change, which shows that the number of grids is independent of the calculation results. Considering the calculation accuracy and efficiency, case 4 is selected as the grid for calculation.

2.4. Evaluation Indexes

In order to better describe the simulated results, some dimensionless parameters for evaluating the integral rolled spiral finned tube bundles are defined. In this study, *Nu* is used to characterize the heat transfer characteristics of the integral rolled spiral finned tube bundles, the larger *Nu*, the stronger the heat transfer. *Eu* is used to characterize the flow resistance characteristics, the larger *Eu*, the higher the flow resistance. PEC is used to characterize the comprehensive heat transfer performance of the integral rolled spiral finned tube bundles, the larger the PEC, the stronger the comprehensive heat transfer performance of the enhanced finned tube bundles compared with the primal finned tube bundles. *ExT* is used to characterize the exergy destruction of the heat transfer processes, the larger *ExT*, the larger the heat transfer exergy destruction. *ExP* is used to characterize the exergy destruction of flow processes, the larger *ExP*, the larger the flow exergy destruction.

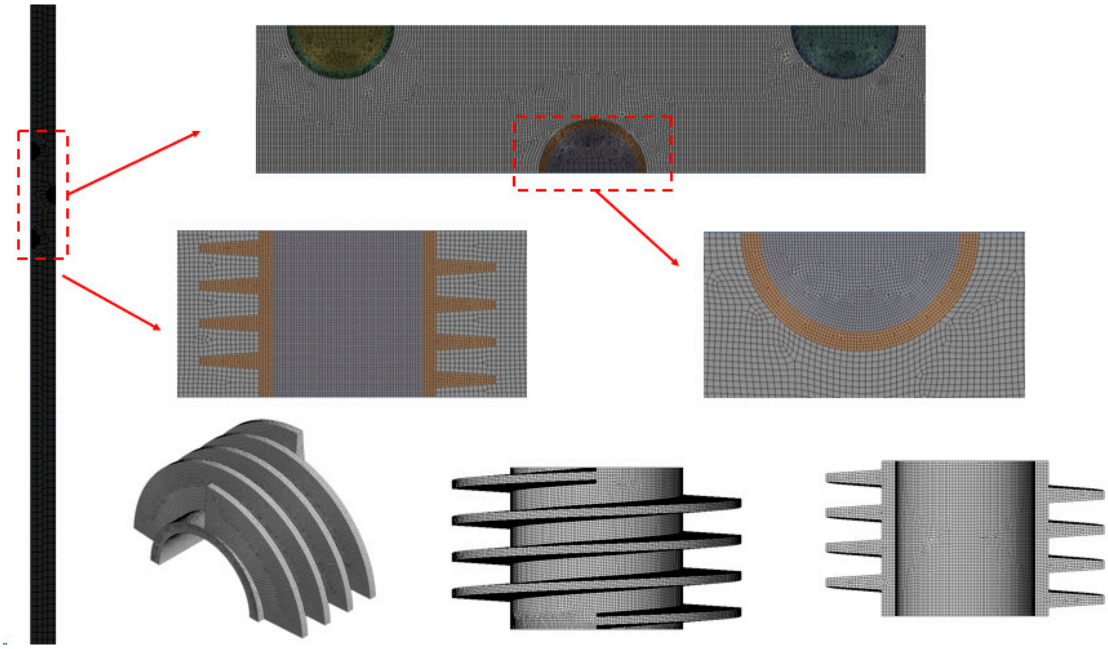

Figure 2. Grid details of the integral rolled spiral finned tube bundles.

Table 2. Grid independence verification.

Case	Number of Grids	Nu_{sim}
1	838,983	57.61
2	1,647,042	58.45
3	2,597,628	59.02
4	3,359,311	59.34
5	4,086,306	59.35

The expressions of Reynolds number (*Re*), Nusselt number (*Nu*) and Euler number (*Eu*) are as follows:

$$Re = \frac{\rho_g u_g d_o}{\mu_g} \tag{10}$$

$$Nu = \frac{h d_o}{\lambda_g} \tag{11}$$

$$Eu = \frac{2\Delta p}{z\rho u_{g,max}^2} \tag{12}$$

ρ_g is the density of the gas, u_g is the velocity of the gas, d_o is the outer diameter of the integral rolled spiral finned tube, μ_g is the viscosity of the gas, h is the heat transfer coefficient, λ_g is the thermal conductivity of the gas, Δp is the differential pressure of the gas, $\Delta p = p_{in} - p_{out}$, $u_{g,max}$ is the maximum velocity of the gas, z is the number of finned tube rows, and $z = 3$ in this study.

In order to better compare the comprehensive heat transfer performance of integral rolled spiral finned tube bundles under different parameters, according to the literature [42], the dimensionless evaluation index PEC is defined, and the expression is as follows:

$$\text{PEC} = \frac{(Nu_e/Nu_p)}{(Eu_e/Eu_p)^{1/3}} \tag{13}$$

In order to quantitatively evaluate the irreversible losses generated in the flow and heat transfer process, according to the literature [36], the heat transfer exergy destruction caused by heat transfer is defined. The expression is as follows:

$$ExT = \iiint_{\Omega} T_0 \frac{\lambda(\nabla T)^2}{T^2} dV \tag{14}$$

The flow exergy destruction caused by gas flow is defined and the expression is as follows:

$$ExP = \iiint_{\Omega} U \cdot (\rho U \nabla U - \mu \nabla^2 U) dV \tag{15}$$

2.5. Experimental System

The physical diagram of the experimental system is shown in Figure 3a, and the schematic diagram of the experimental system is shown in Figure 3b. The whole experimental system consists of centrifugal fan, natural gas, burner, uniform flow orifice plate, reaction equipment, water tank, water pump, exhaust gas treatment system and data collection system. The red route and blue route indicate the flow processes of hot and cold fluids, respectively, and the arrow direction represents the flow direction of the fluid. P, T and F represent pressure sensors, temperature sensors and flowmeters, respectively. The experimental procedure is shown as follows: the quantitative air and natural gas are burned in the combustion chamber. The generated high-temperature flue gas enters the reactor and flows through the uniform flow orifice plate. After heating exchange with the tube bundles, the low temperature gas is fed into the gas treatment system and discharged after treatment. Through the pump, the quantitative cold water enters the tube bundles from the bottom. The cold water has heat exchange with the tube bundles and the generated hot water is discharged from the top of the tube bundles and then returned to the water tank. The water temperature in the water tank is kept stable by adding extra cold water and discharging excess water from the water tank. The experimental equipment has an external insulation layer to reduce the heat exchange between the reactor and the environment, thereby reducing the experimental error.

2.6. Experimental Scheme

The arrangement and section schematic diagram of integral rolled spiral finned tube bundles are shown in Figure 4a. The physical diagram of the integral rolled spiral finned tube is shown in Figure 4b. The influence of structural parameters on the heat transfer and flow resistance characteristics of integral rolled spiral finned tube bundles is obtained by experiments. The custom thermocouples are used to measure the temperature difference between gas and water. The differential pressure transmitters with an accuracy of 0.2% are used to measure the pressure drop of gas. The annular flow meters with an accuracy of 1% are used to measure the flow of gas and the electromagnetic flow meters with an accuracy of 0.5% are used to measure the flow of water. The measurement equipment has been calibrated. The details of the measuring equipment are shown in Table 3 and the uncertainty of the experimental parameters are shown in Table 4. The uncertainty of the experiment can be calculated according to the relationship proposed by Moffa [43].

$$\delta R = \left[\sum_{i=1}^{N} \left(\frac{\partial R}{\partial X_i} \delta X_i \right)^2 \right]^{1/2} \tag{16}$$

where δR is the total uncertainty of the dependent variable R of each measurement parameter X_i, and δX_i is the uncertainty of each independent variable.

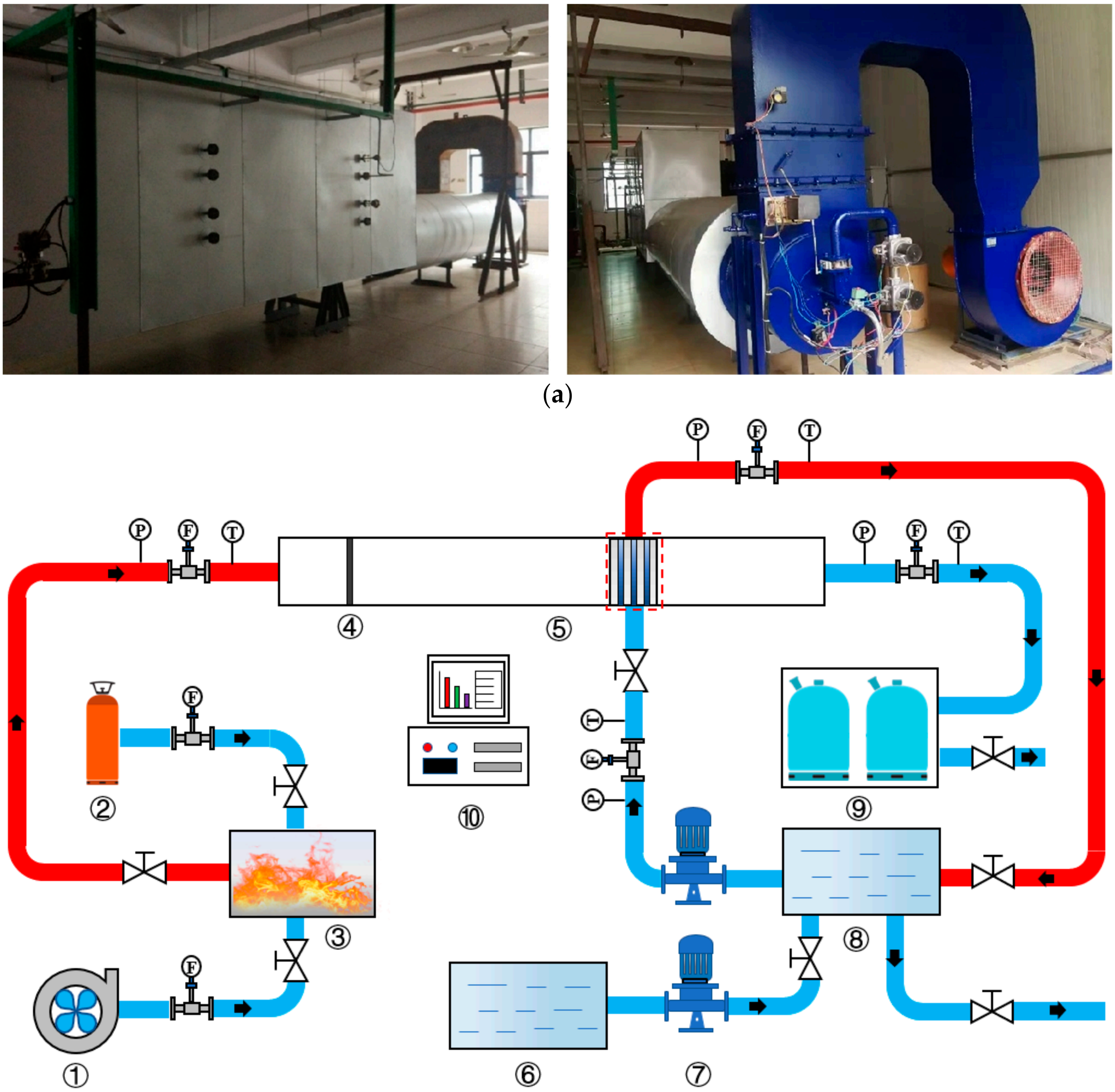

Figure 3. The physical and schematic diagram of the experimental system. (**a**) The physical diagram of the experimental system. (**b**) The schematic diagram of the experimental system. 1. centrifugal fan; 2. natural gas; 3. combustion chamber; 4. uniform flow orifice plate; 5. reaction equipment; 6. cold water tank; 7. pump; 8. water tank; 9. gas treatment system; 10. data acquisition system.

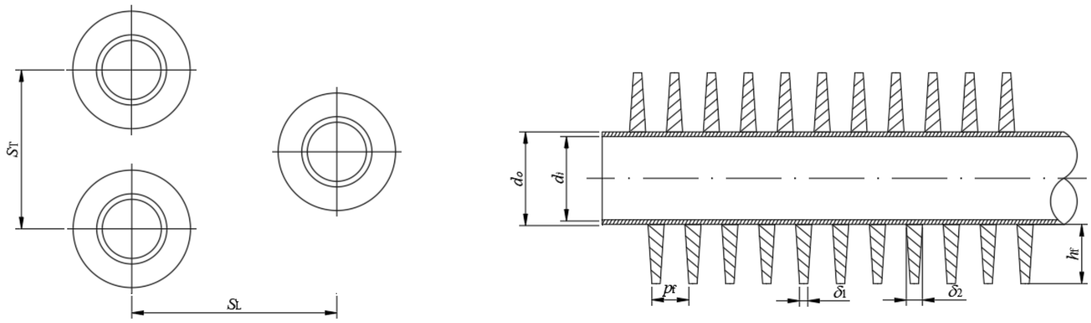

(**a**)

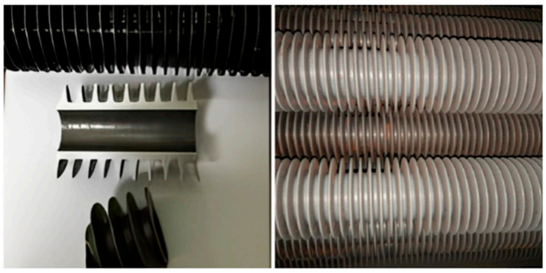

(**b**)

Figure 4. The structure and physical diagram of the integral rolled spiral finned tube bundles. (**a**) The structure diagram of integral rolled spiral finned tube bundles. (**b**) The physical diagram of the integral rolled spiral finned tube bundles.

Table 3. The details of measuring equipment.

Value	Equipment Name	Accuracy	Measuring Range
$u_{g,i}$	Orifice flowmeter	1%	1–15 m/s
P_g	Difference pressure transmitter	0.2%	0.1–1 Kpa
$T_{w,i}$	PT100	A	0–100 °C
$T_{g,i}$	Thermocouple	1.5°C	0–500 °C
$u_{w,i}$	Electromagnetic flowmeter	0.5%	0.1–15 m/s

Table 4. The uncertainty of experimental parameters.

Value	$u_{g,i}$	P_g	$T_{w,i}$	$T_{g,i}$	$u_{w,i}$	*Re*	*Nu*	*Eu*
Uncertainty (%)	4.09	4.74	3.98	6.54	3.28	9.37	8.64	10.26

2.7. Model Validation

In order to verify the reliability and accuracy of the simulated results, the integral rolled spiral finned tube bundles with the same structural parameters were selected for experimental and simulated results comparison. The comparative results of the experimental and simulated *Nu* and *Eu* are exhibited in Figure 5. The experimental and simulated results reveal the same properties. The relative error range of *Nu* is 0.17−5.64% with an average relative error of 2.48% and the relative error range of *Eu* is 5.54−10.01% with an average relative error of 6.90%, which indicates that the mathematical model is accurate and reliable.

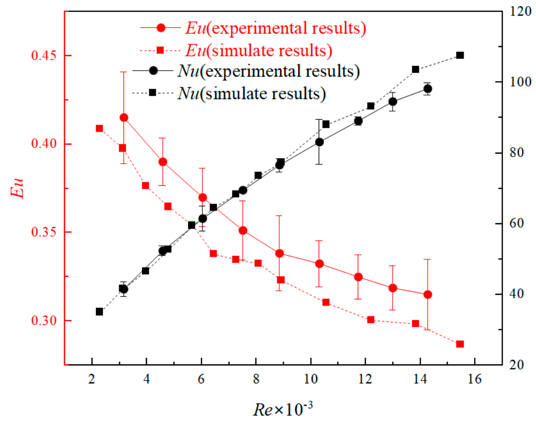

Figure 5. Comparison of experimental and simulated results.

3. Optimization Method

3.1. Data Preprocessing

In this study, the optimization data come from the CFD calculation results. The dimension and magnitude of the data (such as fin tip thickness, fin root thickness and the velocity of gas) are different. In order to improve the stability and convergence rate of the model, the data are normalization processed and the new eigenvalue x^* is obtained, as follows:

$$x^* = \frac{x - x_{\min}}{x_{\max} - x_{\min}} \tag{17}$$

where $x_{\min}$ and $x_{\max}$ are the minimum and maximum eigenvalues of each dimension, respectively. PEC is affected by fin tip thickness, fin root thickness and the velocity of gas. The fin tip thickness, fin root thickness and velocity of gas are input data. PEC is output data. Overall, 80% of the data are used as training data for model training and 20% of the data are used as test data for model testing.

3.2. Prediction Models

Machine learning is an artificial intelligence technique that achieves generalization beyond training samples and successfully interprets unseen data via learning features. In this study, the following four common machine learning algorithms are used to construct the prediction model of PEC. After evaluating their predictive performance, the optimal model among them is used to obtain the optimal parameters of PEC [44–48].

(1) The artificial neural networks (ANN) establish the mapping relationship between the input and output by supervised learning and error back propagation is used to achieve the update iteration of weights and obtain the minimum error and predict the target value. A three-layer neural network with a hidden layer (3-32-1) is used to build a PEC prediction model. The weights and bias are initialized via using the normal random distribution. The training hyperparameter learning rate is defined as 0.001 and the maximum number of iterations is 3000. The mean square error function is used for the loss function and the iteration can be stopped when the error is less than 10^{-4}. The gradient descent method is used for the optimizer.

(2) The random forest regression (RFR) is a flexible and serviceable learning algorithm. The basic principle is to establish multiple different decision trees from the features of the data and calculate the average value of the predicted values of all decision trees to obtain the final predicted value. The RFR has good stability and anti-overfitting ability. In this study, the RFR with 10 decision trees is used for PEC prediction.

(3) The linear regression (LR) is the most commonly used machine learning algorithm. The process of seeking multiple independent variables to affect a dependent variable

through a linear relationship is called multiple regression. The common multiple linear regression model is represented as follows:

$$y = a_0 + a_1 x_1 + a_2 x_2 \cdots\cdots + a_n x_n \tag{18}$$

(4) The support vector machine (SVM) is a set of supervised learning methods used for classification and regression. By establishing an optimal decision hyperplane, the distance between the two types of samples closest to the plane on both sides of the plane is maximized, thus providing good generalization ability for classification and regression problems. In this study, the optimization problem is constructed based on the support vector regression (SVR) model via selecting a suitable kernel function and optimizing the penalty factor c and kernel function parameters. Taking the positive component of α_i* as the support vector (0 < α_i* < c), the optimization function is as follows:

$$b^* = y_j - \sum_{i=1}^{l} \alpha_i^* y_i K(x_i - x_j) \tag{19}$$

The decision function:

$$f(x) = \mathrm{sgn}\left[\sum_{i=1}^{l} \alpha_i^* y_i K(x, x_i) + b^*\right] \tag{20}$$

3.3. Evaluation Indexes of Optimization Models

The R^2 is a dimensionless number used to evaluate the fitting degree of the predicted value and the actual value in the regression model. When the value of R^2 is closer to 1, the higher the correlation between the independent variable and the dependent variable is, and the better the fitting degree is [49]. The specific formula is as follows:

$$R^2 = 1 - \frac{\sum_{i=0}^{m} (y_i - \hat{y}_i)^2}{\sum_{i=0}^{m} (y_i - \overline{y})^2} \tag{21}$$

where y_i is the actual value, $\hat{y}_i$ is the predicted value and $\overline{y}$ is the average value. The mean square error (MSE) is used to evaluate the deviation between the predicted value and the actual value [50,51]. The model is more accurate when MSE is closer to 0. The specific formula is as follows:

$$\mathrm{MSE} = \frac{1}{m} \sum_{i=1}^{m} (y_i - \hat{y}_i)^2 \tag{22}$$

4. Results and Discuss

In this section, simulated results will be presented. The temperature field and flow field will be first introduced. Secondly, the influence of fin root thickness and fin tip thickness on *Nu*, *Eu*, *PEC*, *ExP* and *ExT* will be discussed. Then, the correlation formula of *Nu* and *Eu* will be fitted. Finally, the parameter optimization will be presented.

4.1. Temperature and Velocity Fields

In order to clearly show the flow and heat transfer characteristics of the integral rolled spiral finned tube bundles, the temperature field, velocity field and streamline diagram on a vertical plane of the tube bundles axis are shown in Figures 6 and 7.

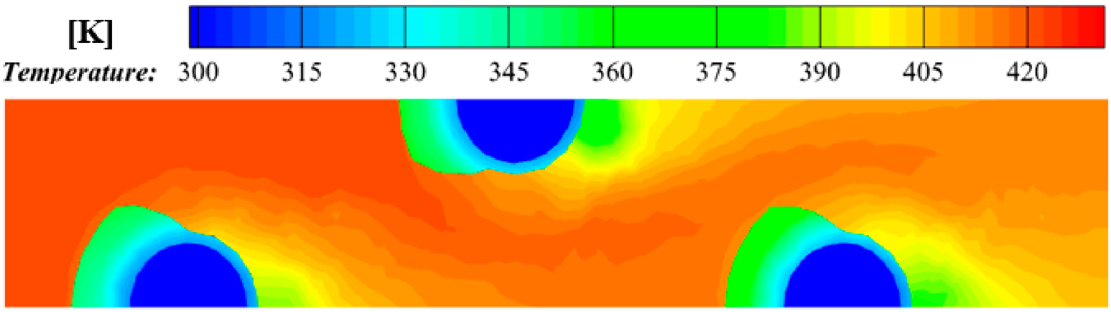

Figure 6. Temperature field on a vertical plane of the tube bundles axis.

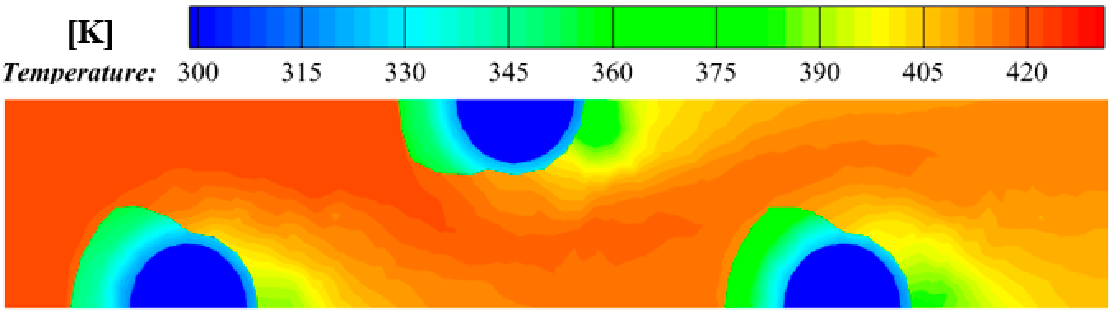

Figure 6. Temperature field on a vertical plane of the tube bundles axis.

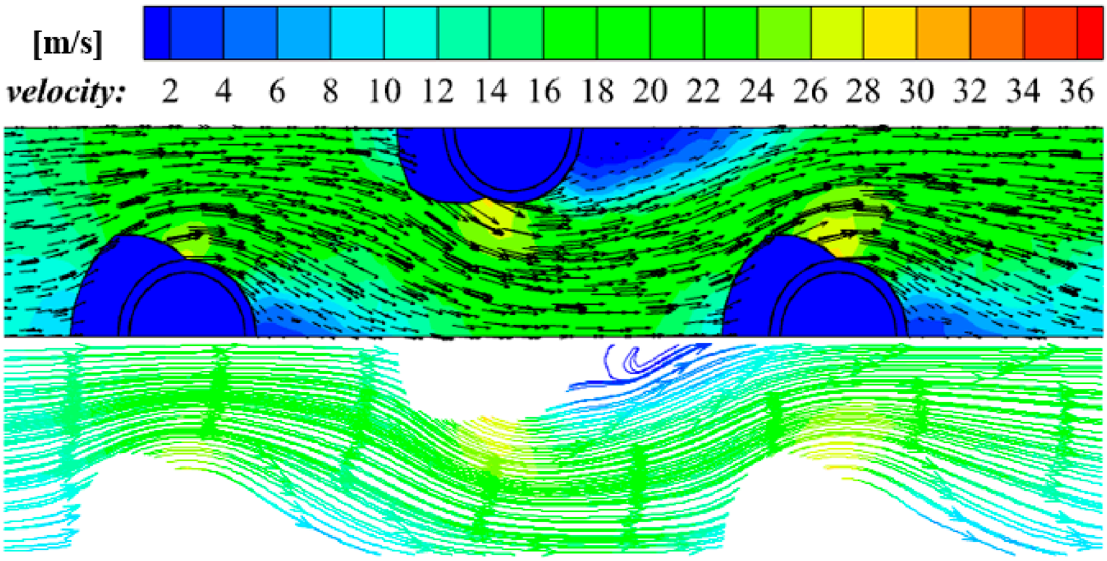

Figure 7. The velocity field and streamline on a vertical plane of the tube bundles axis.

From Figure 6, it can be seen that when the gas scours the integral rolled spiral finned tube bundles, the temperature of gas decreases with the increase in the number of tube rows. Convective heat transfer occurs between the outer wall of the integral rolled spiral finned tube and the gas, and the temperature of the outer wall increases. Thermal conduction occurs between the outer wall and the inner wall of the integral rolled spiral finned tube bundles. It can be seen that the temperature of the tube bundle from the outer wall to the inner wall is gradually reduced. Convective heat transfer occurs between the water and the inner wall of the integral rolled spiral finned tube bundles, and the temperature of water gradually rises. After the gas contacts the tube wall, it will flow along the direction of the tube wall. At this time, the velocity of gas gradually increases until the gas is detached from the integral rolled spiral finned tube bundles. And then the gas after the detachment will flow into the mainstream. Due to the effect of gas detachment, there will be a low temperature zone behind the integral rolled spiral finned tube bundles. The formation of the low temperature zone is not conducive to the heat transfer of the tube bundles.

It can also be seen that when the gas scours through the integral rolled spiral finned tube bundles, the velocity of gas on the front of the windward side decreases. The gas flows along the tube wall, and the velocity of gas gradually increases until the gas is detached from the integral rolled spiral finned tube bundles, which will lead to a low-speed zone of gas at the leeward side of the tube bundles. The formation of the low-speed zone is not conducive to the heat transfer of the integral rolled spiral finned tube bundles. The detached gas will merge with other gases to continue to scour the integral rolled spiral finned tube bundles.

4.2. Effect of Fin Root Thickness and Fin Tip Thickness on Evaluation Indexes

Figure 8 shows the influence of the fin tip thickness and the fin root thickness on the heat transfer characteristics of integral rolled spiral finned tube bundles. Compared with a fin tip thickness of 1.8 mm, when Nu_e/Nu_p is greater than 1, it means that the heat transfer performance of the finned tube bundles with the adjusted parameters is better than that with the primeval parameters. The heat transfer capacity of the integral rolled spiral finned tube bundles shows a downward parabolic trend with the increase in fin tip thickness. When δ_1 = 2 mm, Nu_e/Nu_p reaches the maximum value and Nu is increased by an average of 3.29%. This is because the flow area of gas changes with the increase in fin tip thickness in the range of 1–2 mm. The primary and secondary turbulence near the wall of integral rolled spiral finned tube bundles is enhanced and the temperature is increased, which enhances the heat transfer of the finned tube bundles. When the fin tip thickness is greater than 2 mm, the flow area of gas is too narrow, which reduces the gas disturbance on the surface of the finned tube bundles.

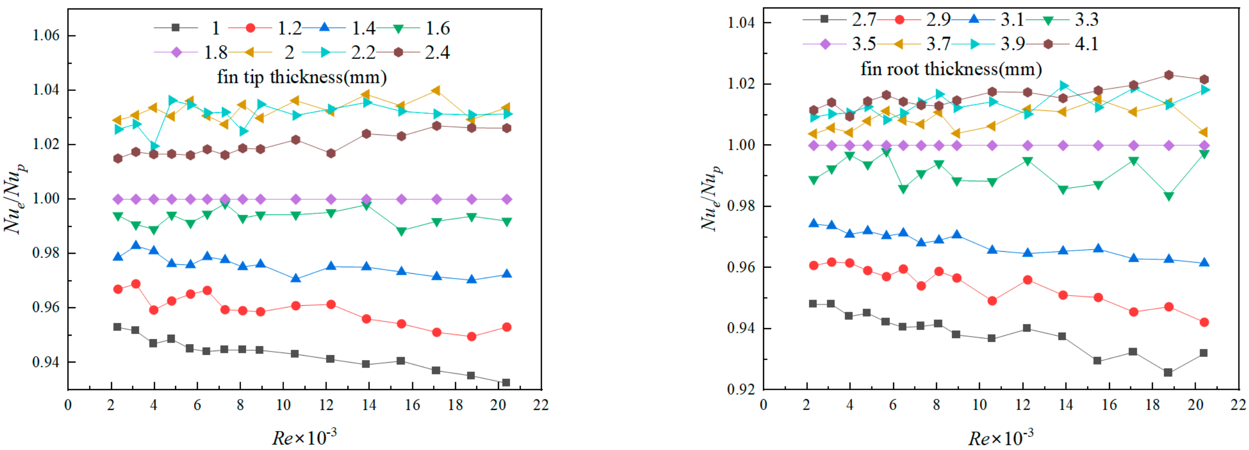

(**a**) (**b**)

Figure 8. Effect of fin root thickness and fin tip thickness on Nu. (**a**) fin tip thickness. (**b**) fin root thickness.

The effect of fin root thickness on Nu is shown in Figure 8b. It can be found that the heat transfer performance of the integral rolled spiral finned tube bundles increases monotonously with the increase in the fin root thickness. When δ_2 = 4.1 mm, the Nu_e/Nu_p reaches the maximum value, and Nu is increased by an average of 1.59%. This is because as the fin root thickness increases, the flow area of gas near the wall becomes narrow, which enhances the disturbance of the gas near the surface of the finned tube bundles and the heat transfer performance.

Figure 9a reveals the influence of the fin tip thickness on the flow resistance characteristics. The results show that the flow resistance increases with the increase in the fin tip thickness, showing a monotonically increasing trend. When δ_1 = 2.4 mm, the maximum value is obtained, and *Eu* is increased by an average of 7.01%. Figure 9b shows the influence of fin root thickness on the flow resistance characteristics. It can be seen from the figure that the flow resistance increases with the increase in fin root thickness, showing a monotonically increasing trend. The reason for these situations is that the increase in the fin tip thickness and fin root thickness reduces the flow area of the gas, which increases the gas velocity and the flow resistance of the gas.

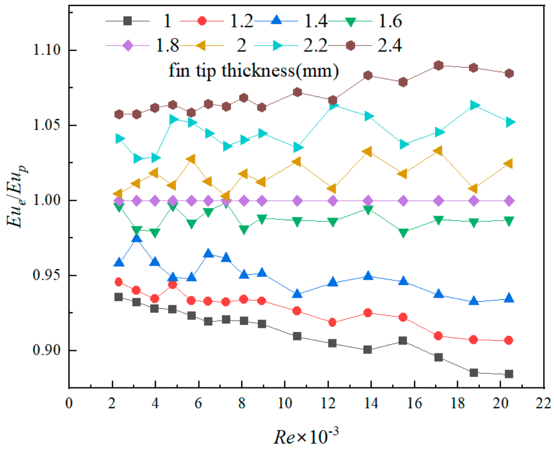

(**a**)

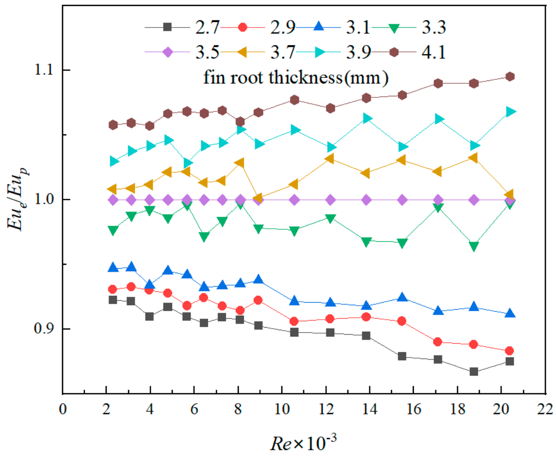

(**b**)

Figure 9. Effect of fin root thickness and fin tip thickness on *Eu*. (**a**) fin tip thickness. (**b**) fin root thickness.

Figure 10 exhibits the effect of fin tip thickness and fin root thickness on PEC, respectively. As shown in Figure 10a, the PEC displays a parabolic trend with the downward opening as fin tip thickness increases in the range of simulated results. The best comprehensive heat transfer performance can be obtained under the condition of a fin tip thickness of 2 mm, with *PEC* being increased by an average of 2.72%. The influence of fin root thickness on PEC is shown in Figure 10b. It can be found that the PEC shows a parabolic trend with the downward opening as fin root thickness increases in the range of simulated results. When the fin root thickness is 3.7 mm, the maximum value is obtained, with an average increase of 0.27%. This also shows that adjusting the fin root thickness has little effect on the comprehensive heat transfer performance of the integral rolled spiral finned tube bundles.

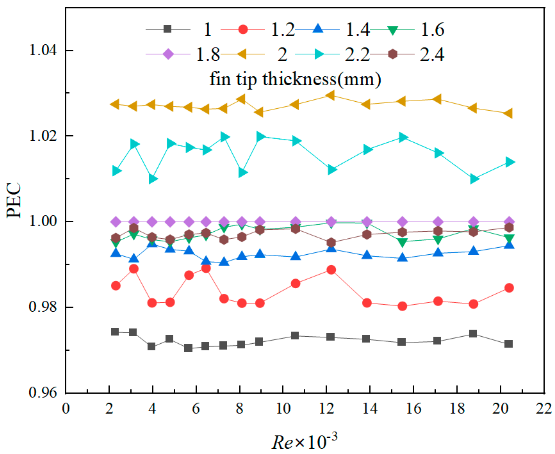

(**a**)

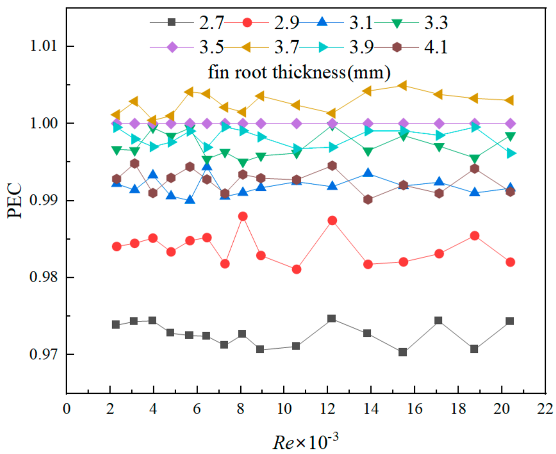

(**b**)

Figure 10. Effect of fin root thickness and fin tip thickness on PEC. (**a**) Fin tip thickness. (**b**) Fin root thickness.

Figure 11a reveals the influence of fin tip thickness on heat transfer exergy destruction. In the range of simulated results, the influence of fin tip thickness on heat transfer exergy destruction shows a trend of decreasing first and then increasing. The minimum heat transfer exergy destruction can be obtained under the condition of a fin tip thickness of 2.2 mm, with the *ExT* being decreased by an average of 12.83%. This regulation of results is consistent with that of *Nu*. The larger the *Nu*, the better the heat transfer performance, and the smaller the heat transfer exergy destruction.

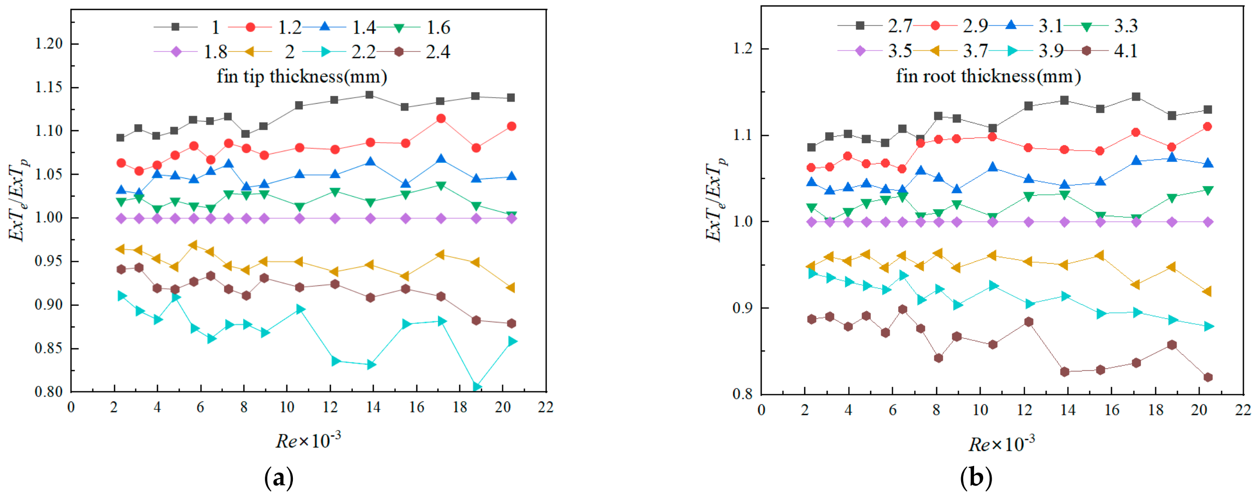

Figure 11. Effect of fin root thickness and fin tip thickness on *ExT*. (**a**) Fin tip thickness. (**b**) Fin root thickness.

The influence of fin root thickness on heat transfer exergy destruction is shown in Figure 11b. In the range of simulated results, the effect of the fin root thickness on heat transfer exergy destruction shows a trend of decreasing first and then increasing. The minimum heat transfer exergy destruction can be obtained under the condition of a fin root thickness of 4.1 mm, with the *ExT* being decreased by an average of 13.63%. The reason for this situation is that the increase in the fin root thickness increases the heat transfer area of the integral rolled spiral finned tube bundles and strengthens the disturbance of the gas, improving the heat transfer performance of the finned tube bundles.

Figure 12a reveals the influence of fin tip thickness on flow exergy destruction. In the range of simulated results, the influence of fin tip thickness on flow exergy destruction shows a monotonically increasing trend. The minimum flow exergy destruction can be obtained under the condition of fin tip thickness of 1 mm, with the *ExP* being decreased by an average of 4.39%. This regulation of results is consistent with that of *Eu*. The larger the *Eu*, the greater the flow resistance, the greater the flow exergy destruction.

The influence of fin root thickness on flow exergy destruction is shown in Figure 12b. In the range of simulated results, the flow exergy destruction increases monotonically with the increase in the fin root thickness. The minimum flow exergy destruction can be obtained under the condition of fin root thickness of 2.7 mm, with the *ExP* being decreased by an average of 7.05%. The reason for this situation is that the increase in fin root thickness reduces the flow area of gas and increases the flow resistance, thus increasing the flow exergy destruction.

4.3. Correlation Formula of Nu and Eu

The dimensionless coefficients δ_1/d_o and δ_2/d_o are used to characterize the influence of the parameters of the integral rolled spiral finned tube bundles on the heat transfer and flow resistance performance. The simulated results are nonlinearly fitted and the heat transfer and flow resistance correlations of integral rolled spiral finned tube bundles are as follows:

$$Nu = 0.433 \times Re^{0.58} Pr^{\frac{1}{3}} \times (\frac{\delta_1}{d_o})^{0.143} \times (\frac{\delta_2}{d_o})^{-0.188} \quad (23)$$

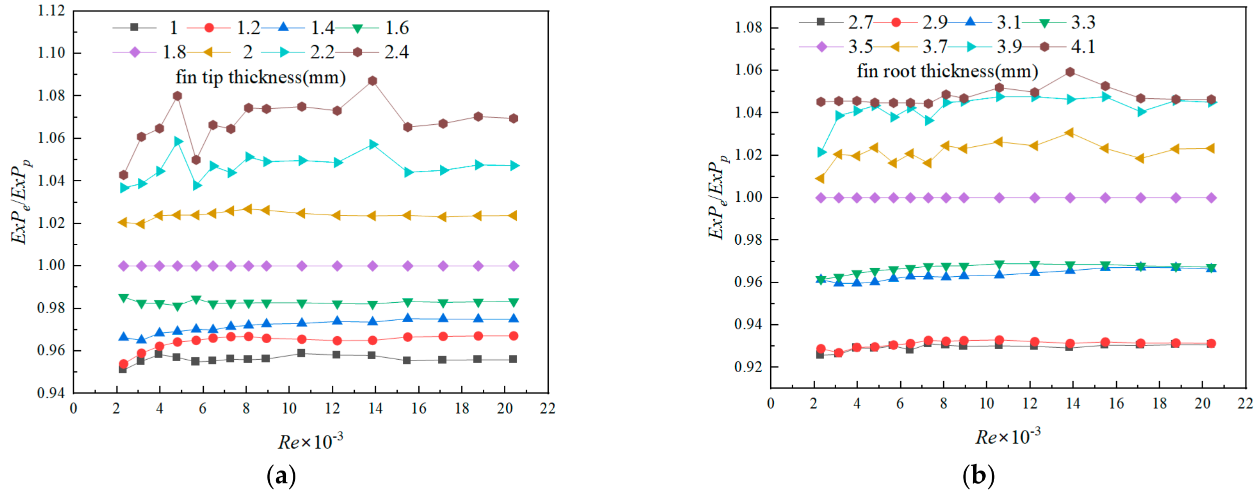

Figure 12. Effect of fin root thickness and fin tip thickness on *ExP*. (**a**) Fin tip thickness. (**b**) Fin root thickness.

The R^2 of Equation (23) is 0.968. Overall, 94.58% of the simulated results have an error of less than 9% from the correlation results. The details are shown in Figure 13a. The sphere of application is as follows: Re = 2287.85–20,375.95, δ_1/d_o = 0.02632–0.06839, δ_2/d_o = 0.07105–0.10790.

$$Eu = 9.993 \times Re^{-0.209} \times (\frac{\delta_1}{d_o})^{0.427} \times (\frac{\delta_2}{d_o})^{0.174} \quad (24)$$

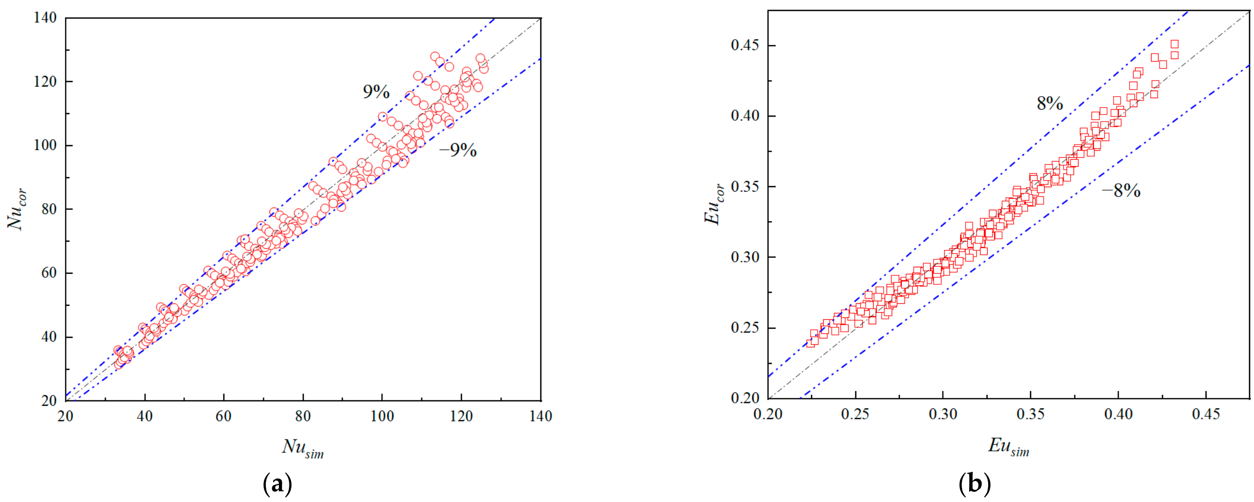

Figure 13. Comparison of simulated results and correlation results. (**a**) *Nu*. (**b**) *Eu*.

The R^2 of Equation (24) is 0.972. Overall, 99.17% of the simulated results have an error of less than 8% from the correlation results. The details are shown in Figure 13b. The sphere of application is as follows: Re = 2287.85–20375.95, δ_1/d_o = 0.02632–0.06839, δ_2/d_o = 0.07105–0.10790.

4.4. Parameter Optimization

Figure 14 shows the comparison between the predicted and actual results of different models. The results of the running different algorithm are shown in Table 5. It can be obviously observed that the R^2 of the SVR model is 0.95 on the training set and only 0.74 on the test set, which is a typical overfitting phenomenon. The LR model and ANN model have a good performance in learning the mapping relationship between data. The RFR model has the best prediction results on the training and test data sets. Considering prediction accuracy, running time and model stability, the RFR model is selected as the algorithm of the PEC prediction model.

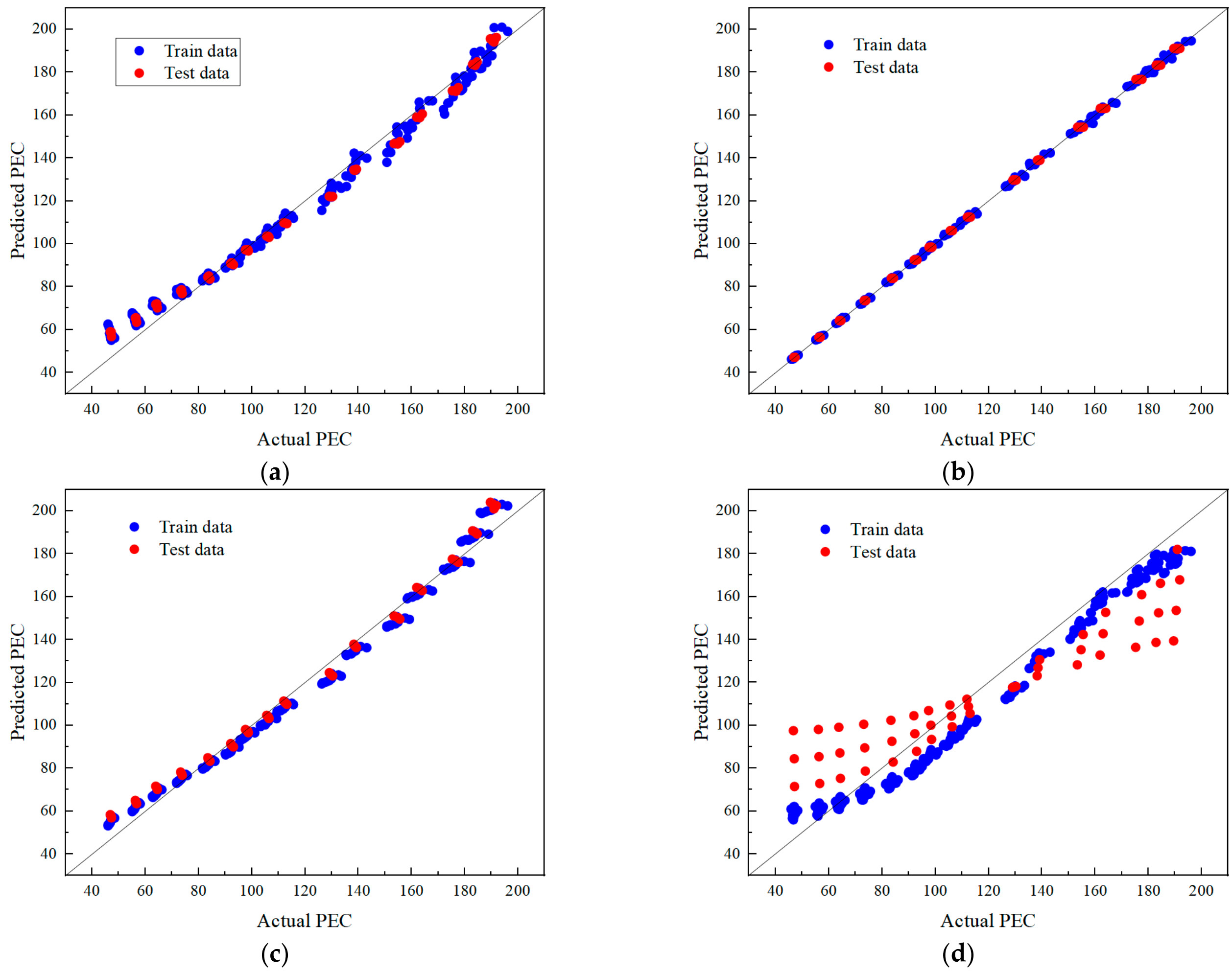

Figure 14. Comparison of predicted and actual results of different models. (**a**) ANN. (**b**) RFR. (**c**) LR. (**d**) SVR.

Table 5. Statistical indicator results of different machine learning models.

Model	MSE (Train)	MSE (Test)	R^2 (Train)	R^2 (Test)
LR	0.001283	0.0014421	0.9859	0.9842
RFR	0.00002045	0.00001640	0.9998	0.9998
SVR	0.004527	0.02306	0.9502	0.7481
ANN	0.001458	0.001351	0.9840	0.9852

Table 6 shows the comparison between the original and optimized parameters. The random function is used to randomly generate 10,000 conditions within the given feature range. These conditions are predicted by RFR model and traversed to obtain the optimal condition combination of PEC. The CFD method is used again to verify the predicted optimal combination results. Compared with the actual PEC (190.09), the deviation of the predicted PEC (194.58) is −0.77%. The results indicate that *Re* has the greatest influence on PEC while fin tip thickness has the least influence on PEC. When δ_1 = 2 mm, δ_2 = 3.5 mm and *Re* = 20,380, the PEC achieves a maximum value of 196.09. When *Re* is the same, compared with the primal parameters, PEC is increased by 2.53%, *ExP* is increased by 2.37%, and *ExT* is decreased by 7.96%.

Table 6. Comparison between the original and optimized parameters.

	δ_1 (mm)	δ_2 (mm)	$u_{g,i}$ (m/s)	PEC	*ExT* (W)	*ExP* (W)
Primal parameters	1.8	3.5	12.3	191.25	1218	4591
Optimization parameters	2	3.5	12.3	196.09	1121	4700

5. Conclusions

In this study, the effects of fin tip thickness and fin root thickness on flow resistance and heat transfer performance and flow and heat transfer exergy destruction are investigated via mathematical simulation. Based on the machine learning, the optimal parameters with PEC as the objective are obtained. The main conclusions are as follows:

(1) The influences of fin tip thickness and fin root thickness on *Nu*, *Eu* and PEC are as follows: with the increase in fin tip thickness, *Nu* presents a parabolic trend with downward opening, *Eu* increases monotonously and PEC shows a parabolic trend with downward opening. With the increase in fin root thickness, *Nu* increases monotonously, *Eu* increases monotonously, and PEC shows a downward opening parabolic trend.

(2) The influences of fin tip thickness and fin root thickness on *ExT*, *ExP* are as follows: with the increase in fin tip thickness, *ExT* shows an upward opening parabolic trend, and *ExP* decreases monotonously. As fin root thickness increases, *ExT* decreases monotonously, and *ExP* decreases monotonously.

(3) A new correlation is proposed for predicting the *Nu* and *Eu* of the integral rolled spiral finned tube bundles in the range of *Re* = 2287.85~20,375.95, δ_1/d_o = 0.02632~0.06839, δ_2/d_o = 0.07105~0.10790.

(4) Four different machine learning algorithms are used to construct the prediction model of PEC, in which the RFR model with the best prediction results is used to optimize the parameters. The optimized parameters fin tip thickness 2 mm and fin root thickness 3.5 mm are obtained via machine learning. Compared with the primal parameters, when the Reynolds number is 20,380, the PEC is increased by 2.53%, the *ExP* is increased by 2.37%, the *ExT* is decreased by 7.96%.

Author Contributions: D.Z.: conceptualization, methodology, writing—original draft. H.D.: supervision, investigation, writing—review and editing. W.W.: data curation. L.Z.: funding acquisition, resources, supervision. All authors have read and agreed to the published version of the manuscript.

Funding: The authors are grateful for the financial support for this work provided by the Science and Technology Program of Zhangjiagang, China (ZKCXY2101), and IGCC/CCPP HRSG Domestic Complete Equipment Green Key Process Technology and System Integration.

Data Availability Statement: Not available.

Conflicts of Interest: The authors declare that they have no known competing financial interests or personal relationships that could have appeared to influence the work reported in this paper.

Nomenclature

h_f—fin height [mm]	p_f—fin pitch [mm]
S_T—transverse pitch [mm]	S_L—longitudinal pitch [mm]
d_i—inner diameter [mm]	d_o—outer diameter [mm]
$u_{g,i}$—velocity of gas inlet [m/s]	$u_{w,i}$—velocity of water inlet [m/s]
$T_{g,i}$—temperature of gas inlet [K]	$T_{w,i}$—temperature of water inlet [K]
ExP—flow exergy destruction [W]	ExT—heat transfer exergy destruction [W]
Greek symbols	
δ_1—fin tip thickness [mm]	δ_2—fin root thickness [mm]
λ_w—thermal conductivity of water [W/(m·K)]	λ_g—thermal conductivity of gas [W/(m·K)]
μ_g—viscosity of gas (Pa·s)	μ_w—viscosity of water (Pa·s)
ρ_g—density of gas (kg/m^3)	ρ_w—density of water (kg/m^3)
Cp_g—specific heat of gas (J/kg·K)	Cp_w—specific heat of water (J/kg·K)

References

1. Miller, W.S.; Zhuang, L.; Bottema, J.; Wittebrood, A.; De Smet, P.; Haszler, A.; Vieregge, A.J.M.S. Recent development in aluminium alloys for the automotive industry. *Mater. Sci. Eng. A* **2000**, *280*, 37–49. [CrossRef]
2. Zhao, D.; Tan, G. A review of thermoelectric cooling: Materials, modeling and applications. *Appl. Therm. Eng.* **2014**, *66*, 15–24. [CrossRef]
3. He, W.; Zhang, G.; Zhang, X.; Ji, J.; Li, G.; Zhao, X. Recent development and application of thermoelectric generator and cooler. *Appl. Energy* **2015**, *143*, 1–25. [CrossRef]
4. Florides, G.; Kalogirou, S. Ground heat exchangers—A review of systems, models and applications. *Renew. Energy* **2007**, *32*, 2461–2478. [CrossRef]
5. Liu, S.; Sakr, M. A comprehensive review on passive heat transfer enhancements in pipe exchangers. *Renew. Sustain. Energy Rev.* **2013**, *19*, 64–81. [CrossRef]
6. Jacobi, A.M.; Shah, R.K. Heat Transfer Surface Enhancement through the Use of Longitudinal Vortices: A Review of Recent Progress. *Exp. Therm. Fluid Sci.* **1995**, *11*, 195–309. [CrossRef]
7. Sheikholeslami, M.; Gorji-Bandpy, M.; Ganji, D.D. Review of heat transfer enhancement methods: Focus on passive methods using swirl flow devices. *Renew. Sustain. Energy Rev.* **2015**, *49*, 444–469. [CrossRef]
8. Kawaguchi, K.; Okui, K.; Kashi, T. Heat transfer and pressure drop characteristics of finned tube banks in forced convection (comparison of the heat transfer characteristics between spiral fin and serrated fin). *Heat Transf. Asian Res.* **2005**, *34*, 120–133. [CrossRef]
9. FaJiang, H.; WeiWu, C.; Ping, Y. Experimental Investigation of Heat Transfer and Flowing Resistance for Air Flow Cross over Spiral Finned Tube Heat Exchanger. *Energy Procedia* **2012**, *17*, 741–749. [CrossRef]
10. Lee, M.; Kang, T.; Kim, Y. Air-side heat transfer characteristics of spiral-type circular fin-tube heat exchangers. *Int. J. Refrig.* **2010**, *33*, 313–320. [CrossRef]
11. Pongsoi, P.; Promoppatum, P.; Pikulkajorn, S.; Wongwises, S. Effect of fin pitches on the air-side performance of L-footed spiral fin-and-tube heat exchangers. *Int. J. Heat Mass Transf.* **2013**, *59*, 75–82. [CrossRef]
12. Pongsoi, P.; Pikulkajorn, S.; Wongwises, S. Experimental Study on the Air-Side Performance of a Multipass Parallel and Counter Cross-Flow L-Footed Spiral Fin-and-Tube Heat Exchanger. *Heat Transf. Eng.* **2012**, *33*, 1251–1263. [CrossRef]
13. Nuntaphan, A.; Kiatsiriroat, T.; Wang, C.C. Air side performance at low Reynolds number of cross-flow heat exchanger using crimped spiral fins. *Int. Commun. Heat Mass Transf.* **2005**, *32*, 151–165. [CrossRef]
14. Nuntaphan, A.; Kiatsiriroat, T.; Wang, C.C. Heat transfer and friction characteristics of crimped spiral finned heat exchangers with dehumidification. *Appl. Therm. Eng.* **2005**, *25*, 327–340. [CrossRef]
15. Boonsri, R.; Wongwises, S. Mathematical Model for Predicting the Heat Transfer Characteristics of a Helical-Coiled, Crimped, Spiral, Finned-Tube Heat Exchanger. *Heat Transf. Eng.* **2015**, *36*, 1495–1503. [CrossRef]
16. Kiatpachai, P.; Pikulkajorn, S.; Wongwises, S. Air-side performance of serrated welded spiral fin-and-tube heat exchangers. *Int. J. Heat Mass Transf.* **2015**, *89*, 724–732. [CrossRef]
17. Zhou, H.; Liu, D.; Sheng, Q.; Hu, M.; Cheng, Y.; Cen, K. Research on gas side performance of staggered fin-tube bundles with different serrated fin geometries. *Int. J. Heat Mass Transf.* **2020**, *152*, 119509. [CrossRef]
18. Salviano, L.O.; Dezan, D.J.; Yanagihara, J.I. Optimization of winglet-type vortex generator positions and angles in plate-fin compact heat exchanger: Response Surface Methodology and Direct Optimization. *Int. J. Heat Mass Transf.* **2015**, *82*, 373–387. [CrossRef]
19. Wen, J.; Gu, X.; Wang, M.; Liu, Y.; Wang, S. Multi-parameter optimization of shell-and-tube heat exchanger with helical baffles based on entransy theory. *Appl. Therm. Eng.* **2018**, *130*, 804–813. [CrossRef]
20. Du, X.; Feng, L.; Yang, Y.; Yang, L. Experimental study on heat transfer enhancement of wavy finned flat tube with longitudinal vortex generators. *Appl. Therm. Eng.* **2013**, *50*, 55–62. [CrossRef]

21. Zhang, J.; Zhao, Y.; Diao, Y.; Zhang, Y. An experimental study on fluid flow and heat transfer in a multiport minichannel flat tube with micro-fin structures. *Int. J. Heat Mass Transf.* **2015**, *84*, 511–520. [CrossRef]
22. He, Y.L.; Han, H.; Tao, W.Q.; Zhang, Y.W. Numerical study of heat-transfer enhancement by punched winglet-type vortex generator arrays in fin-and-tube heat exchangers. *Int. J. Heat Mass Transf.* **2012**, *55*, 5449–5458. [CrossRef]
23. CHEN, J.-Y.J.L.-K. Numerical analysis of heat transfer and fluid flow in a three-dimensional wavy-fin and tube heat exchanger. *Int. J. Heat Mass Transf.* **1997**, *40*, 3981–3990.
24. Li, J.; Wang, S.; Chen, J.; Lei, Y.-G. Numerical study on a slit fin-and-tube heat exchanger with longitudinal vortex generators. *Int. J. Heat Mass Transf.* **2011**, *54*, 1743–1751. [CrossRef]
25. Modi, A.J.; Rathod, M.K. Comparative study of heat transfer enhancement and pressure drop for fin-and-circular tube compact heat exchangers with sinusoidal wavy and elliptical curved rectangular winglet vortex generator. *Int. J. Heat Mass Transf.* **2019**, *141*, 310–326. [CrossRef]
26. Yaïci, W.; Ghorab, M.; Entchev, E. 3D CFD study of the effect of inlet air flow maldistribution on plate-fin-tube heat exchanger design and thermal–hydraulic performance. *Int. J. Heat Mass Transf.* **2016**, *101*, 527–541. [CrossRef]
27. Yuan, F.; Chen, Q. Two energy conservation principles in convective heat transfer optimization. *Energy* **2011**, *36*, 5476–5485. [CrossRef]
28. Yu, Z.-Q.; Wang, P.; Zhou, W.-J.; Li, Z.-Y.; Tao, W.-Q. Study on the consistency between field synergy principle and entransy dissipation extremum principle. *Int. J. Heat Mass Transf.* **2018**, *116*, 621–634. [CrossRef]
29. Wu, X.-H.; Yuan, P.; Luo, Z.-M.; Wang, L.-X.; Lu, Y.-L. Heat Transfer and Thermal Resistance Characteristics of Fin with Built-In Interrupted Delta Winglet Type. *Heat Transf. Eng.* **2015**, *37*, 172–182. [CrossRef]
30. Liu, W.; Liu, P.; Wang, J.B.; Zheng, N.B.; Liu, Z.C. Exergy destruction minimization: A principle to convective heat transfer enhancement. *Int. J. Heat Mass Transf.* **2018**, *122*, 11–21. [CrossRef]
31. Wang, S.; Xiao, B.; Ge, Y.; He, L.; Li, X.; Liu, W.; Liu, Z. Optimization design of slotted fins based on exergy destruction minimization coupled with optimization algorithm. *Int. J. Therm. Sci.* **2020**, *147*, 106133. [CrossRef]
32. Xiao, H.; Wang, J.; Liu, Z.; Liu, W. Turbulent heat transfer optimization for solar air heater with variation method based on exergy destruction minimization principle. *Int. J. Heat Mass Transf.* **2019**, *136*, 1096–1105. [CrossRef]
33. Xie, J.H.; Cui, H.C.; Liu, Z.C.; Liu, W. Optimization design of helical micro fin tubes based on exergy destruction minimization principle. *Appl. Therm. Eng.* **2022**, *200*, 117640. [CrossRef]
34. Vasconcelos Segundo, E.H.d.; Mariani, V.C.; Coelho, L.d.S. Design of heat exchangers using Falcon Optimization Algorithm. *Appl. Therm. Eng.* **2019**, *156*, 119–144. [CrossRef]
35. Li, A.; Ismail, A.B.; Thu, K.; Ng, K.C.; Loh, W.S. Performance evaluation of a zeolite–water adsorption chiller with entropy analysis of thermodynamic insight. *Appl. Energy* **2014**, *130*, 702–711. [CrossRef]
36. Erek, A.; Dincer, I. An approach to entropy analysis of a latent heat storage module. *Int. J. Therm. Sci.* **2008**, *47*, 1077–1085. [CrossRef]
37. Guelpa, E.; Sciacovelli, A.; Verda, V. Entropy generation analysis for the design improvement of a latent heat storage system. *Energy* **2013**, *53*, 128–138. [CrossRef]
38. Lemmon, E.W.; Bell, I.H.; Huber, M.L.; McLinden, M.O. *NIST Standard Reference Database 23: Reference Fluid Thermodynamic and Transport Properties-REFPROP, Version 10.0*; National Institute of Standards and Technology, Standard Reference Data Program: Gaithersburg, MD, USA, 2018. [CrossRef]
39. Mon, M.S.; Gross, U. Numerical study of fin-spacing effects in annular-finned tube heat exchangers. *Int. J. Heat Mass Transf.* **2004**, *47*, 1953–1964. [CrossRef]
40. Oneissi, M.; Habchi, C.; Russeil, S.; Bougeard, D.; Lemenand, T. Novel design of delta winglet pair vortex generator for heat transfer enhancement. *Int. J. Therm. Sci.* **2016**, *109*, 1–9. [CrossRef]
41. Bhuiyan, A.A.; Amin, M.R.; Islam, A.K.M.S. Three-dimensional performance analysis of plain fin tube heat exchangers in transitional regime. *Appl. Therm. Eng.* **2013**, *50*, 445–454. [CrossRef]
42. Webb, R.L. Performance evaluation criteria for use of enhanced heat transfer surfaces in heat exchanger design. *Int. J. Heat Mass Transf.* **1981**, *24*, 715–726. [CrossRef]
43. Moffat, R.J. Describing the uncertainties in experimental results. *Exp. Therm. Fluid Sci.* **1988**, *1*, 3–17. [CrossRef]
44. Baghban, A.; Kahani, M.; Nazari, M.A.; Ahmadi, M.H.; Yan, W.-M. Sensitivity analysis and application of machine learning methods to predict the heat transfer performance of CNT/water nanofluid flows through coils. *Int. J. Heat Mass Transf.* **2019**, *128*, 825–835. [CrossRef]
45. El-Said, E.M.S.; Abd Elaziz, M.; Elsheikh, A.H. Machine learning algorithms for improving the prediction of air injection effect on the thermohydraulic performance of shell and tube heat exchanger. *Appl. Therm. Eng.* **2021**, *185*, 116471. [CrossRef]
46. Fawaz, A.; Hua, Y.; Le Corre, S.; Fan, Y.; Luo, L. Topology optimization of heat exchangers: A review. *Energy* **2022**, *252*, 124053. [CrossRef]
47. Khan, M.Z.A.; Khan, H.A.; Aziz, M. Performance optimization of heat-exchanger with delta-wing tape inserts using machine learning. *Appl. Therm. Eng.* **2022**, *216*, 119135. [CrossRef]
48. Yousefi, M.; Enayatifar, R.; Darus, A.N.; Abdullah, A.H. A robust learning based evolutionary approach for thermal-economic optimization of compact heat exchangers. *Int. Commun. Heat Mass Transf.* **2012**, *39*, 1605–1615. [CrossRef]

49. Peng, Y.; Unluer, C. Modeling the mechanical properties of recycled aggregate concrete using hybrid machine learning algorithms, Resources. *Conserv. Recycl.* **2023**, *190*, 106812. [CrossRef]
50. Wu, W.; Zhang, M.; Wang, Y.; Zhao, L.; Dong, H.; Zhang, J. Optimization of a pyrolysis furnace using multi-jet arrays through numerical and machine learning techniques. *Int. J. Heat Mass Transf.* **2023**, *214*, 124426. [CrossRef]
51. Wu, W.; Zhang, M.; Zhao, L.; Dong, H.; Zhang, J. CFD-DPM data-driven GWO-SVR for fast prediction of nitrate decomposition in blast furnaces with nozzle arrangement optimization. *Process Saf. Environ. Prot.* **2023**, *176*, 438–449. [CrossRef]